

# Correlated helimagnetic configuration in a nonsymmorphic magnetic nodal semimetal

Xi Luo<sup>1,\*</sup>, Yu-Ge Chen<sup>2,\*</sup>, Ye-Min Zhan<sup>3</sup>, and Yue Yu<sup>3†</sup>

1. College of Science,  
University of Shanghai for Science and Technology,  
Shanghai 200093, China

2. Institute for Quantum Science and Technology,  
Physics Department, Shanghai University,  
Shanghai 200444, China

3. State Key Laboratory of Surface Physics and Department of Physics,  
Fudan University, Shanghai 200433, China

(Dated: February 7, 2025)

Nonsymmorphic magnetic Weyl semimetal materials such as ReAlX (Re=rare earth, X=Si/Ge) provide a unique opportunity to explore the correlated phenomena between Weyl fermions and nontrivial magnetic configurations. To be specific, we study a lattice model in which the magnetic configuration is determined by the competition among ferromagnetic (FM) interaction, the Dzyaloshinsky-Moriya interaction, and the Kondo coupling  $K_0$  to the Weyl fermion. Both quantum and finite-temperature phase transitions between FM and correlated nesting helical configurations are found. Different from the uncorrelated helimagnet that decouples to the Weyl fermions, this correlated helimagnet induces a magnetic Brillouin zone with a  $K_0$ -dependent nesting in the band structure of the conducting fermions instead of the magnetic monopole-like Weyl cone. By measuring the current induced by the chiral magnetic effect on the conducting fermion with nesting Weyl nodes, one can distinguish the correlated nesting helical order and the ferromagnetism because the chiral magnetic effect is considerably suppressed in the former case. These properties we study here may explain experimental observations in ReAlX.

*Introduction.* Recently, the nodal semimetals in a set of nonsymmorphic magnetic materials, ReAlX (Re=rare earth, X=Si/Ge), interested in several groups [1–4] and a type of Weyl semimetals with breaking both the time-reversal and inversion symmetries was found in ReAlX [5–14]. These magnetic materials belong to the body-centered tetragonal crystal system with a non-centrosymmetric space group  $I4_1md(109)$ . Due to the inversion symmetry breaking, the Weyl points possess different energies. Meantime, the  $f$ -orbital electrons of the rare earth elements provide a strong magnetic moment, such that a strong Ruderman-Kittel-Kasuya-Yosida (RKKY) interaction can exist by mediating Weyl fermions. The RKKY interaction induces competition among the Heisenberg, Kitaev-Ising, and Dzyaloshinsky-Moriya (DM) interactions [15–17], which leads to the emergence of several non-trivial magnetic configurations, such as spiral, helical, hedgehog, skyrmion, and meron-antimeron pairs [18].

On the other hand, the ReAlX materials provide a unique opportunity to study the correlated phenomena by mediating Weyl fermions, i.e., a platform for studying the interplay between Weyl fermions and non-trivial magnetic configurations through the Kondo coupling [19], e.g., which causes new exotic phenomena such as the topological Hall effect and room temperature anomalous Hall effect [9, 11]. These novel effects make it possible

to prepare high-density ultra-fast storage devices using these materials [20–24].

Physically, these nontrivial magnetic orders rotate the Weyl fermion’s spin configuration in real space via the Kondo coupling, which competes with the monopole topology of the Weyl nodes in momentum space. This competition may further induce new correlated phenomena and correlated topological states of matter that lack clear explanations yet.

In this Letter, we focus on the correlated nesting helical magnetic configuration (CNHMC), which has been observed in many ReAlX materials. For example, since the ratio between out-of-plane and in-plane magnetic susceptibility  $\chi_c/\chi_a$  is very close in SmAlSi at  $2K$ , a helimagnet with  $\mathbf{Q} = \frac{2\pi}{a}(\frac{1}{3} - 0.007, \frac{1}{3} - 0.007, 0)$  emerges ( $a$  is the lattice constant), which is consistent with the nesting vector between Weyl nodes [9]. In CeAlGe, a phase transition from the canted magnetic order to the helimagnet is observed at  $4.5K$ . The helimagnet also provides a nesting vector between the Weyl nodes, and stabilizes magnetic fluctuations above the magnetic transition temperature [8]. This phase transition to the helimagnet and the inducing correlation phenomenon with a nesting vector are also reported in PrAlSi [5], NdAlSi [6], CeAlSi [7], and NdAlGe [10].

However, the origin of the emergence of the CNHMC observed in these materials as well as the mechanism of the magnetic phase transition remains unclear. Particularly, in the materials with multiple Weyl nodes, which nesting condition dominates the magnetic order is still an open question. The specific mechanism behind the anomalous transport phenomena observed near

\*These two authors contribute equally.

†Correspondence to: yuyue@fudan.edu.cn

$T = 12.8\text{K}$  in CeAlGe, such as the nearly zero magnetoresistance, the switch from negative to positive magnetoresistance, and the maximal suppression of thermal conductivity by magnetic fields, is not yet fully understood [8].

In the traditional treatment of the magnetic Weyl semimetal, the magnetic configuration  $\mathbf{M}$  and Weyl fermion are studied separately and the Kondo coupling is treated as a perturbation. However, in ReAlX, the strong Kondo coupling plays an important role so that this separated treatment is not valid. In this Letter, when we deal with the conducting fermion, we take  $\mathbf{M}$  as a background field. When we determine the magnetic configuration, we also assume the magnetic configuration is not fluctuated by the conducting fermion. We see the phase transitions from an ordered phase, e.g., the ferromagnetic (FM) one, to the CNHMC both at zero temperature and finite temperature. We calculate the current induced by the chiral magnetic effect (CME) both in the FM phase and the CNHMC and find that the current in the lattice case is an order of magnitude less than that in the former. This may explain the nearly zero magnetoresistance near  $T = 12.8\text{K}$  in CeAlGe [8].

*Lattice model.* The common model study for the materials ReAlX starts from the calculation of the band structure of this body-centered tetragonal crystal system with a non-centrosymmetric space group  $I4_1md(109)$ . The Weyl nodes are found near the Fermi level and are coupled to the local moment from the  $f$ -electron in the rare-earth element. Such a strategy is fine but is difficult to understand the basic physics due to the complicated numerics.

In order to see the basic physics behind the numerics, we study a simplified cubic lattice model in which both the time-reversal and inversion symmetries are broken. The conducting fermion's Weyl nodes are adjusted to near the Fermi level. The fermions couple to the magnetization via the Kondo coupling while the magnetizations are coupled through the FM Heisenberg and the DM interactions:

$$H = H_W + H_K + H_H + H_{DM}, \quad (1)$$

$$H_W = \sum_j [(-t_x c_j^\dagger \sigma_z c_{j+\hat{x}} - t_y c_j^\dagger \sigma_z c_{j+\hat{y}} - t_z c_j^\dagger \sigma_z c_{j+\hat{z}} - it'_x c_j^\dagger \sigma_x c_{j+\hat{x}} - it'_y c_j^\dagger \sigma_y c_{j+\hat{y}} - iv_0 c_j^\dagger \sigma_0 c_{j+\hat{z}} + h.c.) + mc_j^\dagger \sigma_z c_j], \quad (2)$$

$$H_K = \sum_j K_0 \mathbf{s}_j \cdot \mathbf{M}_j, \quad H_H = \sum_{\langle ij \rangle} J_0 \mathbf{M}_i \cdot \mathbf{M}_j,$$

$$H_{DM} = \sum_{\langle ij \rangle} \mathbf{D}_0 \cdot \mathbf{M}_i \times \mathbf{M}_j.$$

For simplicity, we here restrict  $H_W$  to be a minimal two-band model for a Weyl semimetal with both time-reversal and inversion symmetries breaking [25, 26] and the Weyl nodes located at  $(0, 0, \pm k_0)$  with  $\cos k_0 = (m/2 - t_x - t_y)/t_z$ .  $c_j^\dagger$  (the spin index omitted) is the

creation operator of the conducting fermion at site  $j$ . The fermion spin operator is defined as  $\mathbf{s}_j = \frac{1}{2} c_j^\dagger \boldsymbol{\sigma} c_j$ . For the FM case,  $J_0 < 0$ . In the following, we choose  $t_x = t_y = t_z = t'_x = t'_y = t = 1, m = 5t$  and  $k_0 = \pi/3$ . The chemical potential has been set to zero.  $H_K$  is the on-site Kondo coupling between the conducting fermion spin  $\mathbf{s}$  and the magnetization  $\mathbf{M}$  with the coupling strength  $K_0$ .  $H_H$  and  $H_{DM}$  are the nearest-neighbor FM Heisenberg and DM interactions, respectively.

When solving the conducting fermion problem, we use the adiabatic approximation, i.e., assuming the conducting fermions are fast-moving with respect to the fluctuations of  $\mathbf{M}$ . The magnetization  $\mathbf{M}$  is considered a background. On the other hand, the configuration of  $\mathbf{M}$  is determined by the competition of the variational ground state energies when the conducting fermion spin is assumed to be polarized by the magnetization configuration, the CNHMC or FM.

For the helical magnetic configuration, without loss of generality, one takes

$$\mathbf{M} = (\sin[Qz], \cos[Qz], 0). \quad (3)$$

The Hamiltonian for Weyl fermion with the Kondo coupling becomes

$$\begin{aligned} H_0 &= H_W + H_K \\ &= \sum_{\mathbf{k}, \sigma} [(m - 2t_x \cos k_x - 2t_y \cos k_y \\ &\quad - 2t_z \cos k_z) c_\sigma^\dagger(\mathbf{k}) \sigma_z c_\sigma(\mathbf{k}) + 2t'_x \sin k_x c_\sigma^\dagger(\mathbf{k}) \sigma_x c_\sigma(\mathbf{k}) \\ &\quad + 2t'_y \sin k_y c_\sigma^\dagger(\mathbf{k}) \sigma_y c_\sigma(\mathbf{k}) + 2v_0 \sin k_z c_\sigma^\dagger(\mathbf{k}) \sigma_0 c_\sigma(\mathbf{k}) \\ &\quad + (c_\uparrow^\dagger(k_x, k_y, Q + k_z) (-i \frac{K_0}{2}) c_\downarrow(k_x, k_y, k_z) + h.c.)], \end{aligned} \quad (4)$$

where  $\uparrow$  and  $\downarrow$  are the spin indices. The last term in Eq. (4) is the Kondo coupling between the Weyl fermion and the helical magnetic configuration. Notice that the momentum shift from  $k_z$  to  $k_z \pm Q$  comes from the helical wave number  $Q$ .

*Continuum limit.* Before going to the numerical calculations for the lattice model, we consider the continuum limit of Eq. (4) to show that the correlated helimagnet is an allowed magnetic ground state configuration. When  $|Q| \ll 2|k_0|$ , the low energy effective Hamiltonian for the two Weyl nodes becomes

$$H_{eff} = \int d^3r \sum_{\nu=\pm} (-iv_\nu \psi_\nu^\dagger \boldsymbol{\sigma} \cdot \nabla \psi_\nu + K_0 \mathbf{M} \cdot \mathbf{s}_\nu + \nu b_0) + \dots, \quad (5)$$

where  $\nu$  labels the valley of the Weyl nodes,  $v_\nu$  is the Fermi velocity of the Weyl node  $\nu$ , and  $b_0$  is the energy offset between the two Weyl nodes caused by the inversion symmetry breaking. The "..." terms include the higher-order terms of derivatives and the exchange terms between the local magnetization. Due to the energy offset  $b_0$  between the two Weyl nodes in a non-centrosymmetric

system, we can integrate out one Weyl fermion that is below the chemical potential, say,  $\psi_-$ . The effective Hamiltonian is given by (the constant  $b_0$  is omitted) [8, 27]

$$H_{eff} = \int d^3r \left[ -i(\psi^\dagger \boldsymbol{\sigma} \cdot \nabla \psi + K_0 \mathbf{M} \cdot \mathbf{s}) + \frac{D}{4} \mathbf{M} \cdot \nabla \times \mathbf{M} + \frac{J}{2} (\nabla \mathbf{M})^2 \right], \quad (6)$$

where the suffix  $+$  is omitted;  $J \propto K_0^2 - 2J_0$  and  $D \propto v_- K_0^2 + 4D_0$  [28, 29]. We have set  $\hbar = v_+ = 1$  and neglected the high-order terms. When  $K_0 = 0$ , the ground state configuration of the normalized magnetization is a uncorrelated helimagnet,  $\mathbf{M} = [\mathbf{e}_1 \sin(\mathbf{Q} \cdot \mathbf{r} + \varphi_0) \pm \mathbf{e}_2 \cos(\mathbf{Q} \cdot \mathbf{r} + \varphi_0)]$  with  $Q = |\mathbf{Q}| = |D/2J|$  and  $\mathbf{Q} \propto \mathbf{e}_1 \times \mathbf{e}_2$  [30]. When  $K_0 \neq 0$ , the spin  $\mathbf{s}$  and magnetization  $\mathbf{M}$  are coupled. The equation of motion for  $\psi$  and the ground state configuration of  $\mathbf{M}$  satisfy

$$\begin{aligned} -i\boldsymbol{\sigma} \cdot (\nabla + i\frac{K_0}{2}\mathbf{M})\psi &= E_e \psi, \\ K_0 \mathbf{s} + \frac{D}{2} \nabla \times \mathbf{M} - J \nabla^2 \mathbf{M} &= 0. \end{aligned} \quad (7)$$

In the limit of  $J \rightarrow 0$ , Eqs. (7) are known as the Seiberg-Witten equations in three dimensions [31, 32] and the zero energy solutions of  $(\psi, \mathbf{M})$  are called Seiberg-Witten monopoles. Here we generalize the Seiberg-Witten equation with  $J \neq 0$  [27]. In the correlated case, the helimagnet (3) remains an exact solution but with

$$Q = \frac{D \pm \sqrt{D^2 + 16JK_0}}{4J}, \quad (8)$$

which reduces to the uncorrelated helimagnet or the FM when  $K_0 = 0$ . We see that when  $K_0 \neq 0$ ,  $|\mathbf{Q}|$  is correlated with the Weyl fermions via the Kondo coupling. A band structure of the conducting fermion  $\psi$  is shown in Fig. 1. The helimagnet introduces a magnetic Brillouin zone, and the Seiberg-Witten solutions are localized at the boundaries of the magnetic Brillouin zone. For more details, see Appendix A.

*The CNHMC effects.* When  $\mathbf{Q}$  of the helimagnet forms a commensurate nesting vector between the Weyl nodes, the helimagnet becomes a nesting magnetic configuration. This nesting effect has been used to explain the experimental results in CeAlGe [8]. However, the uncorrelated helimagnet state is not allowed in ReAlX. By considering the CNHMC, the low energy effective Hamiltonian of the conducting fermion reads

$$H'_{eff} = \sum_{\mathbf{k}} \Phi_{\mathbf{k}}^\dagger h'_{\mathbf{k}} \Phi_{\mathbf{k}}, \quad (9)$$

$$\begin{aligned} h'_{\mathbf{k}} &= k'_x \sigma_x \tau_0 + k'_y \sigma_y \tau_0 + k'_z \sigma_z \tau_z \\ &+ a_0 k'_z \sigma_0 \tau_0 + b_0 \sigma_0 \tau_z + K_0 \sigma_y \tau_x / 2, \end{aligned} \quad (10)$$

where  $\Phi = (c_{+\uparrow}, c_{+\downarrow}, c_{-\uparrow}, c_{-\downarrow})$  with  $\pm$  labels two Weyl valleys;  $\sigma$  and  $\tau$  are the matrices that act on spin and valley indices, respectively.  $k'_x = 2t'_x k_x$ ,  $k'_y = 2t'_y k_y$ ,  $k'_z =$

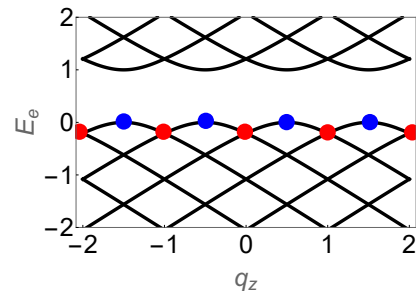


FIG. 1: (color online) The band structure in the continuum limit for Weyl fermions coupled with a helimagnet (3) along  $q_z$ -direction. We set  $Q = K_0 = 1$ . The helimagnet will introduce a magnetic Brillouin zone. The red points stand for the Weyl nodes and the blue points stand for the Seiberg-Witten-type zero modes (see Appendix A).

$2t_z(\sin k_0)k_z$ ,  $a_0 = v_0(\cot k_0)/t$ , and  $b_0 = 2v_0(\sin k_0)$ . The spectra of Hamiltonian (10) read

$$\begin{aligned} E_{\pm, \pm} &= a_0 k'_z \\ &\pm \sqrt{k'^2 + (K_0/2)^2 + b_0^2 \pm \sqrt{K_0^2(k_y'^2 + k_z'^2) + 4b_0^2 k'^2}}. \end{aligned} \quad (11)$$

In the  $K_0 \rightarrow 0$  limit,  $b_0$  becomes the energy offset between the two Weyl nodes, and  $a_0$  controls the type of the Weyl node. When  $b_0 \rightarrow 0$ , the CNHMC does not open a gap but drives the Weyl semimetal to a nodal-ring semimetal when  $k_y'^2 + k_z'^2 = K_0^2/4$ .

*Band structures of the fermion.* Now we turn back to the lattice model. Similar to the treatment of a constant external magnetic field in the lattice model for the IQHE [33–35] (see Appendix B for a brief review), one can define

$$|\Psi\rangle = \sum_{j=1}^q \psi_j c^\dagger(k_x, k_y, k_z^0 + Qj)|0\rangle, \quad (12)$$

where  $Q = 2\pi p/q$  with  $p$  and  $q$  coprime,  $k_z = k_z^0 + Qj$ , and  $\psi_{j+q} = \psi_j$ . Then, the Schrödinger equation  $H_0|\Psi\rangle = E|\Psi\rangle$  is reduced to the Harper equation:

$$\begin{aligned} [m - 2t_x \cos k_x - 2t_y \cos k_y - 2t_z \cos(k_z^0 + Qj)]\sigma_z \psi_j \\ + 2t'_x \sin k_x \sigma_x \psi_j + 2t'_y \sin k_y \sigma_y \psi_j + 2v_0 \sin(k_z^0 + Qj)\sigma_0 \psi_j \\ + (-i\frac{K_0}{2})\psi_{\downarrow, j-1} + (i\frac{K_0}{2})\psi_{\uparrow, j+1} = E(k_x, k_y, k_z^0)\psi_j. \end{aligned} \quad (13)$$

The Harper equation has  $q$  eigenvalues for a given  $(k_x, k_y, k_z^0)$ . The original band for the lattice model is split into  $q$  subbands due to the Kondo coupling to the CNHMC, and each subband has a reduced magnetic Brillouin zone:  $-\pi \leq k_x, k_y \leq \pi$  and  $-\pi/q \leq k_z^0 \leq \pi/q$ .

In ReAlX, the Fermi velocity near the Weyl node is of the order of  $1eV\text{\AA}$ , and the lattice constant is of the order of  $10\text{\AA}$ . Therefore, the hopping constant  $t \sim 100meV$ . The Curie temperature is about  $30K$ , then,  $|J_0| \sim 2.5meV$ . In the first-principles calculations,

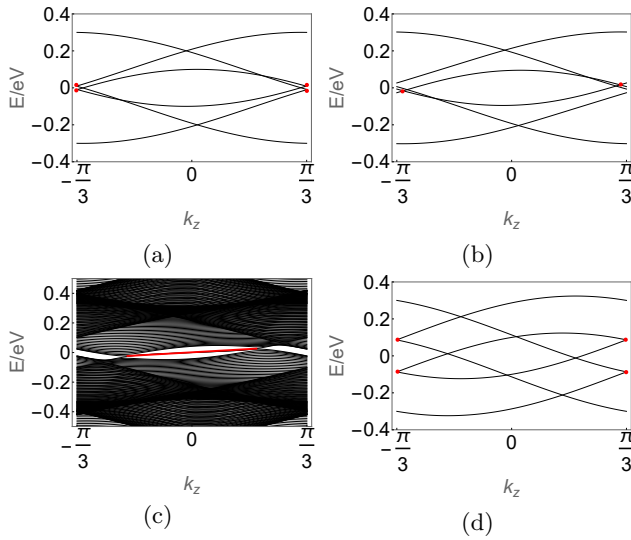


FIG. 2: (color online) The band structures of Weyl fermions with CNHMC  $Q = 2\pi/3$ .  $t = t' = 0.1\text{eV}$  and  $k_x = k_y = 0$ . (a)  $K_0 = 10\text{meV}$ ,  $v_0 = 5\text{meV}$ . (b)  $K_0 = 50\text{meV}$ ,  $v_0 = 5\text{meV}$ . (c)  $K_0 = 200\text{meV}$ ,  $v_0 = 5\text{meV}$  with open boundary conditions of 50 sites along  $y$ -axis. (d)  $K_0 = 10\text{meV}$ ,  $v_0 = 50\text{meV}$ . The red points in (a), (b), and (d) label the Weyl nodes. The red line in (c) stands for the Fermi arc. One sees that the Weyl nodes will get closer as  $K_0$  increases and they eventually annihilate and open a gap.

the Kondo coupling and DM interaction are of the same order as the Heisenberg interaction  $|K_0| \sim |D_0| \sim |J_0|$  [5–14]. We choose similar parameters and use exact diagonalization to plot the band structure of  $H_0$  (4) with the CNHMC in Fig. 2. We find that, for the commensurate nesting  $Q = 2\pi/3$ , the Weyl nodes are folded to the boundaries of the magnetic Brillouin zone for a small  $K_0$  (see Fig. 2a). If  $K_0$  increases, the Weyl nodes will move towards each other (see Fig. 2b), which may explain the slightly incommensurate behavior of the helimagnetic configuration observed in experiments. For a strong enough  $K_0$ , the Weyl nodes will merge together and open a gap. And the Fermi arcs that connect the Weyl nodes will also evolve from shortening to disappearing. (see Fig. 2c). On the other hand, the inversion-breaking term  $v_0$  will shift the energy of every Weyl node, but it does not alter the locations of the Weyl nodes (see Fig. 2d).

*Magnetic phase diagram.* We turn to study the magnetic phase diagrams of the model Hamiltonian (1). For a fixed magnetic configuration, here which is either the FM or the CNHMC, we compare the ground state energy per site at zero temperature and the free energy  $f$  per site at finite temperature of Eq. (1). For the CNHMC, one take  $Q = 2\pi/3$  and the FM is given by  $Q = 0$ . To obtain the spectra, we use exact diagonalization in the calculations and choose periodic boundary conditions for a lattice with 20 sites in all directions, i.e.,  $L_x = L_y = L_z = 20$ .

At zero temperature, we find that for a fixed  $J_0$ , the

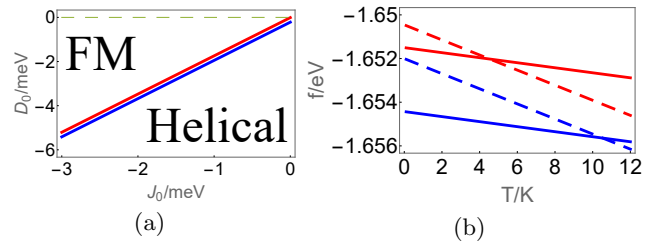


FIG. 3: (color online) The parameters are the same as in Fig. 2a except for  $K_0$ .  $K_0 = 10\text{meV}$  for the red lines and  $K_0 = 50\text{meV}$  for the blue lines. (a) The zero temperature phase diagram between the FM and the CNHMC. The gray dashed line stands for the case with  $D_0 = 0$  for which the ground state energy per site is the same for both phases along the lines. Above (below) the lines, the FM (helical) configuration is energetically favored. (b) The free energy per site,  $f$ , for finite temperature with  $J_0 = -3\text{meV}$  and  $D_0 = -4\text{meV}$ . The solid (dashed) lines stand for  $f$  of the FM (helical) configuration.

CNHMC is favored for large DM interaction  $D_0$ . The phase boundary moves downward when  $K_0$  increases (see Fig. 3a). And for finite temperature, by choosing  $J_0 = -3\text{meV}$ ,  $D_0 = -4\text{meV}$ ,  $K_0 = 10\text{meV}$ , with the other parameters the same as those in Fig. 2a, a phase transition occurs at about  $T_c = 4.5\text{K}$  (Fig. 3b), which is qualitatively consistent with experiments in [8], although the ordered phase is a canted magnetic order instead of the FM. By increasing  $K_0$ , the transition temperature also lifts (see Fig. 3b).

*CME with CNHMC.* To further explore the effects of the CNHMC in this type of magnetic Weyl semimetals, we study the CME [36]. For an isolated Weyl node given by the low-energy Hamiltonian  $h_w = b_0 + \boldsymbol{\sigma} \cdot (\mathbf{k} - \mathbf{b})$ , where  $\mathbf{b}$  and  $b_0$  denote the shift in momentum and energy, respectively. Its response to the external magnetic field is described by the topological  $\theta$ -term,  $\theta_{\mathbf{x},t} \mathbf{E} \cdot \mathbf{B}$ , with  $\theta_{\mathbf{x},t} = 2(\mathbf{b} \cdot \mathbf{x} - b_0 t)$  [37–40], which originates from the chiral anomaly of the Weyl fermion [41–43] and corresponds to the charge density  $\rho \propto \mathbf{b} \cdot \mathbf{B}$  and current  $\mathbf{j} \propto (\mathbf{b} \times \mathbf{E} - b_0 \mathbf{B})$ . The  $\mathbf{b}$ -related terms contribute to the anomalous Hall effect, while the  $b_0$  term contributes to the CME which is related to the giant negative magnetoresistance [44–47]. In our model Hamiltonian  $H_0$  (4),  $b_0 \propto v_0$  and  $\mathbf{b} \propto (0, K_0, 0)$  in the FM limit  $Q = 0$ . For the CNHMC with  $|Q| = 2|k_0|$ ,  $\mathbf{b}$  is not well-defined for small  $K_0$  because the Weyl nodes are close to each other due to band-folding.

To consider the CME in the magnetic nodal semimetal with the CNHMC, we apply a uniform magnetic field in the  $z$ -direction in the model Hamiltonian (4). In the  $x$ - $y$  plane, we label the lattice sites by  $(n, m)$  and choose the gauge  $\theta_{(n,m),(n+1,m)}^x = 0$  for the link between  $(n, m)$  and  $(n+1, m)$ , and  $\theta_{(n,m),(n,m+1)}^y = 2\pi\phi n$  [33–35]. This gauge gives a uniform magnetic field whose flux through a unit plaquette is  $2\pi\phi$  (here we have set  $c = e = 1$  and the flux quantum  $\phi_0 = 1$ ). Then the current in the CME

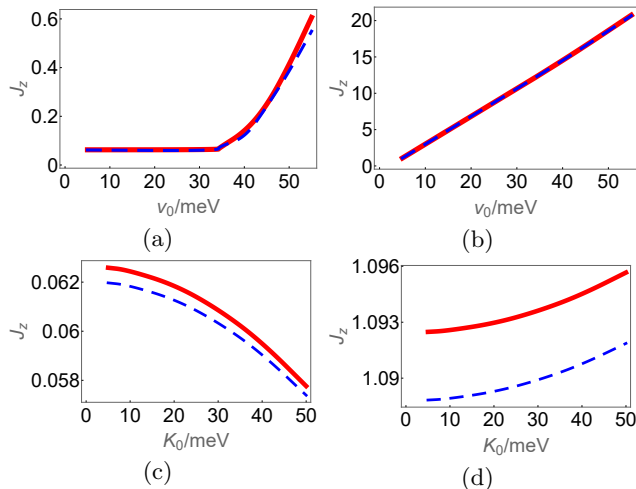


FIG. 4: (color online) The current  $J_z$  of the CME at zero temperature. We choose the hopping constants  $t = t' = 0.1eV$ , the magnetic flux  $\phi = 1/5$ , and lattice size  $L_x = 20$  with periodic boundary condition for the red solid lines and open boundary condition for the blue dashed lines. The cutoff of  $k_z$  is chosen as  $\Lambda = \pi/6$ . (a)  $K_0 = 10meV$ ,  $Q = 2\pi/3$ ; (b)  $K_0 = 10meV$ ,  $Q = 0$ ; (c)  $v_0 = 5meV$ ,  $Q = 2\pi/3$ ; (d)  $v_0 = 5meV$ ,  $Q = 0$ .

reads [44]

$$J_z = \sum_{n,k_y,k_z} \langle \phi_{n,k_y,k_z} | \frac{\partial H_0(k_z)}{\partial k_z} | \phi_{n,k_y,k_z} \rangle n_F(E_n(k_y, k_z)) \quad (14)$$

where  $n_F$  is the Fermi-Dirac distribution function and the gauge choice is included in  $H_0$ . We choose periodic boundary conditions in  $y$ - and  $z$ -directions. Both periodic and open boundary conditions are considered for  $x$ -direction with a length  $L_x$ . We set  $\phi = 1/5$ .

We then calculate  $J_z$  for various system sizes and boundary conditions; the results are zero within the numerical accuracy if the entire (magnetic) Brillouin zone is taken into account. This is consistent with the fact that to drive a current in a metal, a nonequilibrium distribution of charge carriers is necessary. On the other hand, the CME can be reproduced by choosing a cutoff  $\Lambda \ll \pi$  in the summation of  $k_z$ , and the current grows linearly

in  $b_0$  for a Weyl semimetal [44]. With this scenario, we calculate the CME with  $L_x = 20$ ,  $\Lambda = \pi/6$ , and plot  $J_z$  by varying  $v_0$  and  $K_0$  at zero temperature in Fig. 4. We find that the surface arc states will have a negative contribution to  $J_z$  because  $J_z$  in the open boundary condition is slightly smaller than the periodic one. In the FM case,  $J_z$  is linearly dependent on  $v_0$  as expected (see Fig. 4b). While for the CNHMC,  $J_z$  remains constant when  $v_0 < 3K_0$  and then grows (see Fig. 4a). For large  $v_0$ , the folded Weyl nodes are separated far enough and isolated (see Fig. 2d). Therefore, the linear behavior of  $J_z$  verse  $v_0$  is expected. And in the  $J_z$  constant regime,  $J_z$  decreases when  $K_0$  increases. This shows that the Kondo coupling will suppress the CME with the CNHMC (see Fig. 4c) while it increases the CME with the FM order (see Fig. 4d). Another key difference between these two magnetic configurations is that the CME in the CNHMC is about 20 times smaller than the FM order, which may explain the fast drop of the magnetoresistance from large negative to positive and nearly zero behavior observed near  $T = 12.8K$  in CeAlGe [8].

*Conclusions.* We considered a minimal lattice model with Kondo, Heisenberg, and DM interactions for the Weyl semimetal that breaks both time-reversal and inversion symmetries, which may be related to the correlated physics in ReAlX. We found that the CNHMC induces a magnetic Brillouin zone in the band structure of conducting fermions. The magnetic phase transitions from the ordered phase to the CNHMC were explored. We also calculated the CME with the CNHMC, which is about 20 times smaller than that with the FM order. This may provide an explanation for the anomalous transport phenomena and nearly zero magnetoresistance observed in CeAlGe.

In this work, we only solved the magnetic Weyl semimetal with the helimagnetic and FM configurations. More kinds of magnetic configurations, such as antiferromagnet, spiral, and skyrmions, were observed in ReAlX materials, which will be of interest in our further research.

We thank Long Liang, and Yong-Shi Wu for helpful discussions. This work is supported by the National Natural Science Foundation of China with Grant No. 12174067 (XL, YMZ, and YY).

- 
- [1] S.-Y. Xu, N. Alidoust, G.-Q. Chang, H. Lu, B. Singh, I. Belopolski, D. S. Sanchez, X. Zhang, G. Bian, H. Zheng, M.-A. Husanu, Y. Bian, S.-M. Huang, C.-H. Hsu, T.-R. Chang, H.-T. Jeng, A. Bansil, T. Neupert, V. N. Strocov, H. Lin, S. Jia, M. Z. Hasan, “Discovery of Lorentz-violating type II Weyl fermions in LaAlGe”, *Sci. Adv.* **3**, e1603266 (2017).
- [2] G.-Q. Chang, B. Singh, S.-Y. Xu, G. Bian, S.-M. Huang, C.-H. Hsu, I. Belopolski, N. Alidoust, D. S. Sanchez, H. Zheng, H. Lu, X. Zhang, Y. Bian, T.-R. Chang, H.-T. Jeng, A. Bansil, H. Hsu, S. Jia, T. Neupert, H. Lin, and

- M. Z. Hasan, “Magnetic and noncentrosymmetric Weyl fermion semimetals in the RAlGe family of compounds (R = rare earth)”, *Phys. Rev. B* **97**, 041104(R) (2018).
- [3] D. S. Sanchez, G. Chang, I. Belopolski, H. Lu, J.-X. Yin, N. Alidoust, X. Xu, T. A. Cochran, X. Zhang, Y. Bian, S. S. Zhang, Y.-Y. Liu, J. Ma, G. Bian, H. Lin, S.-Y. Xu, S. Jia, and M. Z. Hasan, “Observation of Weyl fermions in a magnetic non-centrosymmetric crystal”, *Nat. Commun.* **11**, 3356 (2020).
- [4] D. Destrz, L. Das, S. S. Tsirkin, Yang Xu, T. Neupert, J. Chang, A. Schilling, A. G. Grushin, J. Kohlbrecher,

- L. Keller, P. Puphal, E. Pomjakushina and J. S. White, “Magnetism and anomalous transport in the Weyl semimetal PrAlGe: possible route to axial gauge fields”, *npj Quantum Mater.* **5**, 5 (2020).
- [5] H.-Y. Yang, B. Singh, B. Lu, C.-Y. Huang, F. Bahrami, W.-C. Chiu, D. Graf, S.-M. Huang, B. Wang, H. Lin, D. Torchinsky, A. Bansil, and F. Tafti, “Transition from Intrinsic to Extrinsic Anomalous Hall Effect in the FM Weyl Semimetal PrAlGe<sub>1-x</sub>Si<sub>x</sub>”, *APL Mater.* **8**, 011111 (2020).
- [6] J. Gaudet, H.-Y. Yang, S. Baidya, B. Lu, G. Xu, Y. Zhao, J. A. Rodriguez-Rivera, C. M. Hoffmann, D. E. Graf, D. H. Torchinsky, P. Nikolić, D. Vanderbilt, F. Tafti, and C. L. Broholm, “Weyl-mediated helical magnetism in NdAlSi”, *Nat. Mater.* **20**, 1650 (2021).
- [7] H.-Y. Yang, B. Singh, J. Gaudet, B. Lu, C.-Y. Huang, W.-C. Chiu, S.-M. Huang, B. Wang, F. Bahrami, B. Xu, J. Franklin, I. Sochnikov, D. E. Graf, G. Xu, Y. Zhao, C. M. Hoffman, H. Lin, D. H. Torchinsky, C. L. Broholm, A. Bansil, and F. Tafti, “Noncollinear FM Weyl Semimetal with Anisotropic Anomalous Hall Effect”, *Phys. Rev. B* **103**, 115143 (2021).
- [8] N. C. Drucker, T. Nguyen, F. Han, P. Siriviboon, X. Luo, N. Andrejevic, Z. Zhu, G. Bednik, Q. T. Nguyen, Z. Chen, L. K. Nguyen, T. Liu, T. J. Williams, M. B. Stone, A. I. Kolesnikov, S. Chi, J. Fernandez-Baca, C. S. Nelson, A. Alatas, T. Hogan, A. A. Puretzky, S. Huang, Y. Yu, and M. Li, “Topology stabilized fluctuations in a magnetic nodal semimetal”, *Nat. Commun.* **14**, 5182 (2023).
- [9] X. Yao, J. Gaudet, R. Verma, D. E. Graf, H.-Y. Yang, F. Bahrami, R. Zhang, A. A. Aczel, S. Subedi, D. H. Torchinsky, J. Sun, A. Bansil, S.-M. Huang, B. Singh, P. Blaha, P. Nikolić, and F. Tafti, “Large Topological Hall Effect and Spiral Magnetic Order in the Weyl Semimetal SmAlSi”, *Phys. Rev. X* **13**, 011035 (2023).
- [10] H.-Y. Yang, J. Gaudet, R. Verma, S. Baidya, F. Bahrami, X. Yao, C.-Y. Huang, L. DeBeer-Schmitt, A. A. Aczel, G. Xu, H. Lin, A. Bansil, B. Singh, and F. Tafti, “Stripe helical magnetism and two regimes of anomalous Hall effect in NdAlGe”, *Phys. Rev. Materials* **7**, 034202 (2023).
- [11] A. Laha, A. K. Kundu, N. Aryal, E. S. Bozin, J. Yao, S. Paone, A. Rajapitamahuni, E. Vescovo, T. Valla, M. Abeykoon, R. Jing, W. Yin, A. N. Pasupathy, M. Liu, and Q. Li, “Electronic structure, magnetic and transport properties of antiFM Weyl semimetal GdAlSi”, *Phys. Rev. B* **109**, 035120 (2024).
- [12] N. Kikugawa, S. Uji, and T. Terashima, “Anomalous Hall effect in the magnetic Weyl semimetal NdAlGe with plateaus observed at low temperatures”, *Phys. Rev. B* **109**, 035143 (2024).
- [13] J. Nag, B. Das, S. Bhowal, Y. Nishioka, B. Bandyopadhyay, S. Kumar, K. Kuroda, A. Kimura, K. G. Suresh, and A. Alam, “GdAlSi: An antiFM topological Weyl semimetal with non-relativistic spin splitting”, *Phys. Rev. B* **110**, 224436 (2024).
- [14] Y. Gao, S. Lei, E. M. Clements, Y. Zhang, X.-J. Gao, S. Chi, K. T. Law, M. Yi, J. W. Lynn, and E. Morosan, “Anomalous Hall effect in the antiFM Weyl semimetal SmAlSi”, arXiv: 2310.09364.
- [15] H.-R. Chang, J. Zhou, S.-X. Wang, W.-Y. Shan, and D. Xiao, “RKKY interaction of magnetic impurities in Dirac and Weyl semimetals”, *Phys. Rev. B* **92**, 241103(R) (2015).
- [16] J.-H. Sun, D.-H. Xu, F.-C. Zhang, and Y. Zhou, “Magnetic impurity in a Weyl semimetal”, *Phys. Rev. B* **92**, 195124 (2015).
- [17] S.-X. Wang, H.-R. Chang, and J. Zhou, “RKKY interaction in three-dimensional electron gases with linear spin-orbit coupling”, *Phys. Rev. B* **96**, 115204 (2017).
- [18] B. Göbel, I. Mertig, O. A. Tretiakov, “Beyond skyrmions: Review and perspectives of alternative magnetic quasiparticles”, *Physics Reports* **895**, 1 (2021).
- [19] A. K. Mitchell and L. Fritz, “Kondo effect in three-dimensional Dirac and Weyl systems”, *Phys. Rev. B* **92**, 121109(R) (2015).
- [20] B. A. Bernevig, C. Felser, and H. Beidenkopf, “Progress and prospects in magnetic topological materials”, *Nature* **603**, 41 (2022).
- [21] Z. Wang, Y. Su, S.-Z. Lin, and C. D. Batista, “Meron, Skyrmion, and Vortex Crystals in Centrosymmetric Tetragonal Magnets”, *Phys. Rev. B* **103**, 104408 (2021).
- [22] . Repicky, P.-K. Wu, T. Liu, J. P. Corbett, T. Zhu, S. Cheng, A. S. Ahmed, N. Takeuchi, J. Guerrero-Sanchez, M. Randeria, R. K. Kawakami, and J. A. Gupta, “Atomic-Scale Visualization of Topological Spin Textures in the Chiral Magnet MnGe”, *Science* **374**, 1484 (2021).
- [23] S. Luo and L. You, “Skyrmion Devices for Memory and Logic Applications”, *APL Mater.* **9**, 050901 (2021).
- [24] V. Rogers, S. Chaudhary, R. Nguyen, and J. A. Incorvia, “Flat bands and multi-state memory devices from chiral domain wall superlattices in magnetic Weyl semimetals”, arXiv:2303.16918.
- [25] F.-Y. Li, X. Luo, X. Dai, Y. Yu, F. Zhang, and G. Chen, “Hybrid Weyl semimetal”, *Phys. Rev. B* **94**, 121105(R) (2016).
- [26] T. M. McCormick, I. Kimchi, and N. Trivedi, “Minimal models for topological Weyl semimetals”, *Phys. Rev. B* **95**, 075133 (2017).
- [27] Y. Yu, “Seiberg-Witten monopoles: Weyl metal coupled to chiral magnets”, arXiv: 1605.00093.
- [28] H.-R. Chang, J. H. Zhou, S.-X. Wang, W.-Y. Shan, and D. Xiao, “RKKY interaction of magnetic impurities in Dirac and Weyl semimetals”, *Phys. Rev. B* **92**, 241103 (2015).
- [29] M. V. Hosseini and M. Askari, “Ruderman-Kittel-Kasuya-Yosida interaction in Weyl semimetals”, *Phys. Rev. B* **92**, 224435 (2015).
- [30] N. Nagaosa, X. Z. Yu, Y. Tokura, “Gauge fields in real and momentum spaces in magnets: monopoles and skyrmions”, *Phil. Trans. R. Soc. A* **370**, 5806 (2012).
- [31] N. Seiberg and E. Witten, “Electric-magnetic duality, monopole condensation, and confinement in  $N = 2$  supersymmetric Yang-Mills theory”, *Nucl. Phys. B* **426**, 19 (1994).
- [32] S. K. Donaldson, “The Seiberg-Witten equations and 4-manifold topology”, *Bull. (New Series) of the Amer. Math. Society*, **33**, 45 (1996).
- [33] M. Kohmoto, “Zero modes and the quantized Hall conductance of the two-dimensional lattice in a magnetic field”, *Phys. Rev. B* **39**, 11943 (1989).
- [34] Y. Hatsugai and M. Kohmoto, “Energy spectrum and the quantum Hall effect on the square lattice with next-nearest-neighbor hopping”, *Phys. Rev. B* **42**, 8282 (1990).
- [35] Y. Hatsugai, “Edge states in the integer quantum Hall effect and the Riemann surface of the Bloch function”,

- Phys. Rev. B **48**, 11851 (1993).
- [36] K. Fukushima, D. E. Kharzeev, and H. J. Warringa, "Chiral magnetic effect", Phys. Rev. D **78**, 074033 (2008).
- [37] A. A. Zyuzin and A. A. Burkov, "Topological response in Weyl semimetals and the chiral anomaly", Phys. Rev. B **86**, 115133 (2012).
- [38] D. T. Son and N. Yamamoto, "Berry Curvature, Triangle Anomalies, and the Chiral Magnetic Effect in Fermi Liquids", Phys. Rev. Lett. **109**, 181602 (2012).
- [39] P. Goswami and S. Tewari, "Axionic field theory of (3+1)-dimensional Weyl semimetals", Phys. Rev. B **88**, 245107 (2013).
- [40] A. G. Grushin, "Consequences of a condensed matter realization of Lorentz-violating QED in Weyl semi-metals", Phys. Rev. D **86**, 045001 (2012).
- [41] S. L. Adler, "Axial-Vector Vertex in Spinor Electrodynamics", Phys. Rev. **177**, 2426 (1969).
- [42] J. S. Bell and R. Jackiw, "A PCAC puzzle:  $\pi_0 \rightarrow \gamma\gamma$  in the  $\sigma$ -model", Il Nuovo Cimento A **60**, 47 (1969).
- [43] H. B. Nielsen, and M. Ninomiya, "The Adler-Bell-Jackiw anomaly and Weyl fermions in a crystal", Physics Letters B **130**, 389 (1983).
- [44] M. M. Vazifeh and M. Franz, "Electromagnetic Response of Weyl Semimetals", Phys. Rev. Lett. **111**, 027201 (2013).
- [45] A. Burkov, "Chiral anomaly and transport in Weyl metals", Journal of Physics: Condensed Matter **27**, 113201 (2015).
- [46] D. T. Son and B. Z. Spivak, "Chiral anomaly and classical negative magnetoresistance of Weyl metals", Phys. Rev. B **88**, 104412 (2013).
- [47] X. Huang, L. Zhao, Y. Long, P. Wang, D. Chen, Z. Yang, H. Liang, M. Xue, H. Weng, Z. Fang, X. Dai, and G. Chen, "Observation of the Chiral-Anomaly-Induced Negative Magnetoresistance in 3D Weyl Semimetal TaAs", Phys. Rev. X **5**, 031023 (2015).

## Appendix A: Solutions for the generalized Seiberg-Witten equations

The equations of motion (EOM) for the Weyl fermion  $\psi$  and the ground state of magnetic order  $\mathbf{M}$  satisfy the generalized Seiberg-Witten equations [27, 31, 32]

$$-i\boldsymbol{\sigma} \cdot (\nabla + i\frac{K_0}{2}\mathbf{M})\psi = E_e\psi, \quad (\text{A1})$$

$$K_0\mathbf{s} + \frac{D}{2}\nabla \times \mathbf{M} - J\nabla^2\mathbf{M} = 0. \quad (\text{A2})$$

Consider the following ansatz,

$$\mathbf{A} = \frac{K_0}{2}\mathbf{M}, \quad (\text{A3})$$

$$\mathbf{M} = (0, \cos[Qx], \sin[Qx]), \quad (\text{A4})$$

$$\mathbf{B}_0 = (\pm)\nabla \times \mathbf{A} = -(\pm)\frac{QK_0}{2}\mathbf{M}, \quad (\text{A5})$$

$$\chi = \frac{1}{\sqrt{2(B_0 + B_{03})}} \begin{pmatrix} B_0 + B_{03} \\ B_{01} + iB_{02} \end{pmatrix}. \quad (\text{A6})$$

One can check  $\mathbf{B}_0 = \chi^\dagger\boldsymbol{\sigma}\chi$  and  $B_0 = \chi^\dagger\chi$ . Therefore this provides a map from  $SU(2)$  to  $SO(3)$ . Then the EOM for  $\psi = \chi/\sqrt{\chi^\dagger\chi}$  reduces to

$$\left(-\frac{Q}{2} - \frac{K_0}{2}\right)\psi = E_e\psi, \quad (\text{A7})$$

and the ground state equation for  $\mathbf{M}$  reduces to

$$K_0\mathbf{M} + \frac{DQ}{2}\mathbf{M} - JQ^2\mathbf{M} = 0. \quad (\text{A8})$$

Therefore one obtains

$$Q = \frac{D \pm \sqrt{D^2 + 16JK_0}}{4J}. \quad (\text{A9})$$

We shall emphasize that although the helical configuration here have the same form as the case for  $K_0 = 0$ ,  $|\mathbf{Q}|$  is correlated with the Weyl fermions via the Kondo coupling. We present a more concrete solution with the ansatz  $\mathbf{M} = \frac{Q}{K}(\sin[Qz], \cos[Qz], 0)$ . Assuming the periodic boundary condition, the spectrum  $E$  of the fermions is determined by solving the equation of motion under the effective Hamiltonian (A1),

$$(-i\boldsymbol{\sigma} \cdot \nabla + \boldsymbol{\sigma} \cdot \frac{K}{2}\mathbf{M})\psi = E\psi. \quad (\text{A10})$$

In order to find the zero energy solution, we focus along one direction, say, z-axis, and take the following ansatz of wave function,

$$\begin{aligned} \psi_0(\mathbf{r}) &= \psi_n(z) \\ &\propto e^{i(k_z + nQ)z} \begin{pmatrix} 1 \\ -\frac{2i}{K}(k_z + nQ - E)e^{-iQz} \end{pmatrix}, \end{aligned} \quad (\text{A11})$$

where  $k_z$  is the wave vector along the z-axis,  $Q$  is the magnetic wave vector of the magnetization, and  $n$  labels the  $n$ th magnetic Brillouin zone determined by  $Q$ . Then, through a direct calculation, the spectrum reads

$$E_{\pm} = \frac{Q}{2} \pm \sqrt{(k_z + (n + \frac{1}{2})Q)^2 + \frac{K^2}{4}}. \quad (\text{A12})$$

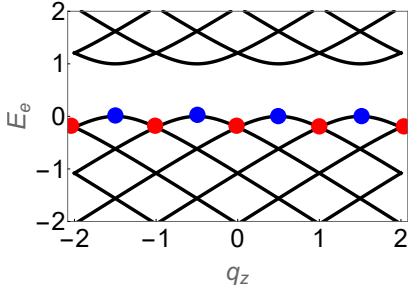


FIG. 5: (color online) The band structure of Eq. (A12) with different  $ns$ .  $Q = K = 1$ . The magnetic Brillouin zone is introduced by the helical magnetic order. The red points stand for the Weyl nodes and the blue points stand for the Seiberg-Witten-type zero modes.

The zero energy occurs when  $|Q| = |K|$  (which is consistent with the normalization  $|\mathbf{M}| = 1$ ), and  $k_z = -(n + \frac{1}{2})Q$ . We plot a diagram of the spectra (A12) in Fig. 5. The spin of these zero modes are the same, i.e.,  $\mathbf{s}_n = \mathbf{s} = \frac{1}{2} \frac{Q}{K} \mathbf{M}$ . Eq. (A2) determines  $Q$  as

$$\frac{Q}{2K} + \frac{DQ}{2K} - \frac{JQ^2}{K} = 0 \Rightarrow Q = \frac{1}{2J}(1 + D), \quad (\text{A13})$$

which also gives a constraint between  $K$  and  $J/D$ . For a pinned helimagnet with  $Q > 0$ , say, in the  $z$  direction, the dispersion near  $k_z = -(n + \frac{1}{2})Q$  for a given zero mode reads,

$$E_-(k_z) \approx -\frac{1}{|K|}(k_z + (n + \frac{1}{2})Q)^2 \equiv -\frac{1}{|K|}q_z^2. \quad (\text{A14})$$

We now do the perturbation by taking  $H_1 = k_x \sigma^x + k_y \sigma^y$  because for the pinned helimagnet, the Hamiltonian (6) in the main text is translational invariant in the  $x$ - $y$  plane. The first order perturbation is zero. The matrix elements between

$$\begin{aligned} \psi_{n-}(z) &\propto e^{i(k_z + nQ)z} \begin{pmatrix} 1 \\ -\frac{i2}{K}(k_z + nQ - E_{n-})e^{-iQz} \end{pmatrix} \\ &= e^{i(k_z + nQ)z} \begin{pmatrix} 1 \\ A_n e^{-iQz} \end{pmatrix} \end{aligned}$$

and  $\psi_{n'-}(z)$  are

$$\begin{aligned} &\langle \psi_{n'-}(z) | H_1 | \psi_{n-}(z) \rangle \\ &= \delta_{n,n'+1} A_n (k_x - ik_y) + \delta_{n,n'-1} A_{n'} (k_x + ik_y). \end{aligned} \quad (\text{A15})$$

The energy differences at  $k_z = -(n + \frac{1}{2})Q$  are

$$E_-(n, k_z) - E_-(n \pm 1, k_z) = \frac{\sqrt{5} - 1}{2} K, \quad (\text{A16})$$

The second order perturbation gives

$$\begin{aligned} E_-^{(2)} &= \sum_{n' \neq n} \frac{\langle \psi_{n-}(z) | H_1 | \psi_{n'-}(z) \rangle \langle \psi_{n'-}(z) | H_1 | \psi_{n-}(z) \rangle}{E_n - E_{n'}} \\ &= \frac{2}{\sqrt{5} - 1} \frac{k_x^2 + k_y^2}{K}. \end{aligned} \quad (\text{A17})$$

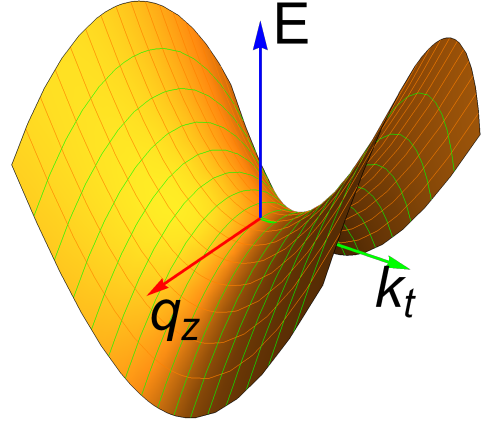


FIG. 6: (color online) A schematic diagram for the dispersion of  $E_-$  (A18) near the blue points in Fig. 5.  $K = 1$ . The dispersion is of a saddle shape. It is a parabola along  $k_t$  and a downward one along  $q_z$ .

Thus, the dispersions near  $k_z = -(n + 1/2)Q$  are

$$\begin{aligned} E_-(\mathbf{k}) &= -\frac{1}{K}q_z^2 + \frac{2}{(\sqrt{5} - 1)K}k_t^2 \\ &\equiv -\frac{q_z^2}{2m_z} + \frac{k_t^2}{2m_t} = -\varepsilon_z + \varepsilon_t, \end{aligned} \quad (\text{A18})$$

with  $\mathbf{k}_t = (k_x, k_y)$ . The dispersion is of a saddle shape (see Fig. 6), namely, in the  $z$  direction is hole-type while in the  $x$ - $y$  plane is particle-type. This means that the dynamics in parallel to the helimagnet and the perpendicular to the helimagnet is separated.

## Appendix B: Two-dimensional lattice model in a constant external magnetic field and Harper equation

Consider a tight-binding Hamiltonian on the square lattice in a magnetic field [33–35],

$$\begin{aligned} H &= -t_a \sum_{\langle i,j \rangle} c_{x,j}^\dagger c_{x,i} e^{i\theta_{ij}^x} \\ &\quad - t_b \sum_{\langle i,j \rangle} c_{y,j}^\dagger c_{y,i} e^{i\theta_{ij}^y} + h.c., \end{aligned} \quad (\text{B1})$$

where  $\theta_{ij}$  is the phase factor of the gauge field which satisfies  $\sum_{\square} \theta_{ij} = 2\pi\phi$  in a unit cell, and  $\phi = p/q$  with  $p, q$  coprime.  $t_a$  and  $t_b$  are the nearest-neighbor hopping constants. A site  $i$  on the square lattice has a Cartesian coordinate  $(n, m)$  where  $n$  and  $m$  are integers. We choose the gauge  $\theta_{ij}^x = 0$ , and  $\theta_{ij}^y = 2\pi\phi n$  for the link between  $i = (n, m)$  and  $j = (n, m + 1)$ . This gauge gives a uniform magnetic field whose flux through a plaquette is  $2\pi\phi$ . In

the momentum space,

$$\begin{aligned}
H(\mathbf{k}) = & -2t_a \cos k_x c^\dagger(k_x, k_y) c(k_x, k_y) \\
& -t_b [e^{-ik_y} c^\dagger(k_x + 2\pi\phi, k_y) c(k_x, k_y) \\
& + e^{ik_y} c^\dagger(k_x - 2\pi\phi, k_y) c(k_x, k_y)], \quad (\text{B2})
\end{aligned}$$

where  $-\pi \leq k_x, k_y \leq \pi$ . Since  $k_x$  is coupled to  $k_x \pm 2\pi\phi$ , the Schrödinger equation  $H|\Psi\rangle = E|\psi\rangle$  is reduced to the Harper equation:

$$\begin{aligned}
& -t_b (e^{-ik_y} \psi_{j-1} + e^{ik_y} \psi_{j+1}) - 2t_a \cos(k_x^0 + 2\pi\phi j) \psi_j \\
& = E(k_x^0, k_y) \psi_j, \quad (\text{B3})
\end{aligned}$$

where  $k_x = k_x^0 + 2\pi\phi j$  and  $\phi_{j+q} = \phi_j$ . And the state  $|\Psi\rangle$  is

$$|\Psi\rangle = \sum_{j=1}^q \psi_j c^\dagger(k_x^0 + 2\pi\phi j, k_y) |0\rangle. \quad (\text{B4})$$